

Calcium niobate nanosheets as a novel electron transport material for solution-processed multi-junction polymer solar cells†

Lilian Chang,^a Michael A. Holmes,^b Mollie Waller,^b Frank E. Osterloh^b and Adam J. Moule^{*a}

Received 24th May 2012, Accepted 8th August 2012

DOI: 10.1039/c2jm33351a

Solution-processed tandem polymer solar cells are demonstrated using stacked perovskite, (TBA,H)Ca₂Nb₃O₁₀ (CNO), semiconductor nanosheets as an electron transport layer (ETL) within the recombination layers. Two poly(3-hexylthiophene):(6,6)-phenyl-C₆₁-butyric acid methyl ester, P3HT:PCBM, sub-cells connected in series *via* a CNO–poly(3,4-ethylenedioxythiophene):poly(styrenesulfonate), Pedot:PSS, recombination layer provide a V_{oc} of 1.02 V. The V_{oc} is less than double that of a single junction due to leakage (dark) current. When TiO_x is used as an additional hole-blocking layer within the recombination stack, the V_{oc} is improved to 1.16 V. Although further optimization of the CNO-layer is still required, the use of CNO nanosheets within the recombination stack shows clear advantages. In addition to electron extraction from photoactive layers, the presence of defect states in the CNO nanosheets with trapped electrons facilitates the recombination of holes from Pedot:PSS, enhancing the function of the recombination stack. The robust CNO-layer can be spin-coated on top of a P3HT:PCBM bulk-heterojunction photoactive layer and is stable toward subsequent processing and heat-treatment.

1 Introduction

Despite significant advances in the design and synthesis of conjugated polymers for use in organic photovoltaic (OPV) devices, polymers still suffer from a limited absorption range, preventing efficient photon harvesting from the full solar spectrum. Additionally, OPV devices are plagued by shorter exciton diffusion lengths and lower charge carrier mobilities compared to their inorganic counterparts,¹ which limits the layer thickness and, consequently, photon absorption. One promising solution to this problem is to stack multiple photoactive layers with complementary absorption spectra (*i.e.* complementary band gaps, E_g). The current reported record efficiency for a tandem polymer solar cell is 10.6%.² While there has been an upsurge of interest in tandem polymer PV and device efficiencies have been rapidly escalating, there is still tremendous opportunity for improvement.

The tandem strategy minimizes thermalization losses by converting high-energy photons in the front sub-cell with a wide band gap polymer ($E_{g,donor}$), while the lower energy photons are absorbed in the back sub-cell with a small $E_{g,donor}$, minimizing transmission losses.³ Since the sub-cells are connected in series, Kirchhoff's law dictates that equal current flows through each

sub-cell, while the voltage across the device is the summation of the individual voltages of the sub-cells.^{4,5} Hence, optimization of a tandem OPV involves not only ensuring the highest efficiency for each sub-cell but also matching the current between the sub-cells.

A successful tandem architecture requires the incorporation of a transparent recombination layer-stack between photoactive layers to prevent a build-up of charges. The photoactive layer is usually a bulk-heterojunction (BHJ), in which the electron donor (conjugated polymer) and electron acceptor (fullerene) are deposited from a common solvent. Nanoscale interpenetrating networks are formed as the donor and acceptor phase-separate during solvent evaporation, yielding charge-separating heterojunctions^{6,7} throughout the photoactive layer. The recombination stack typically consists of an electron transport layer (ETL) and a hole transport layer (HTL). In a standard configuration (transparent indium-doped tin oxide (ITO)-coated glass as an anode), as shown in Fig. 1, the ETL extracts electrons from the front cell while the HTL collects holes from the back cell. These charges have to meet at the same energy level at the ETL–HTL interface to avoid voltage losses, *i.e.* the ETL and HTL have to be in ohmic contact with each other.⁸ Charge selectivity of the ETL and HTL is very important to ensure effective charge extraction from the BHJ photoactive layers. Fabrication of tandem devices through solution-processing further requires that the solvent used for subsequent layer deposition be innocuous to the underlying layer, and that the surface energies of the layers be compatible to ensure wetting and complete layer coverage. Solution-processed tandem OPV devices have also been

^aDepartment of Chemical Engineering and Materials Science, University of California, One Shields Avenue, Davis, CA 95616, USA. E-mail: amoule@ucdavis.edu; Fax: +1-530-752-1031; Tel: +1-530-754-8669

^bDepartment of Chemistry, University of California, Davis, USA

† Electronic supplementary information (ESI) available. See DOI: 10.1039/c2jm33351a

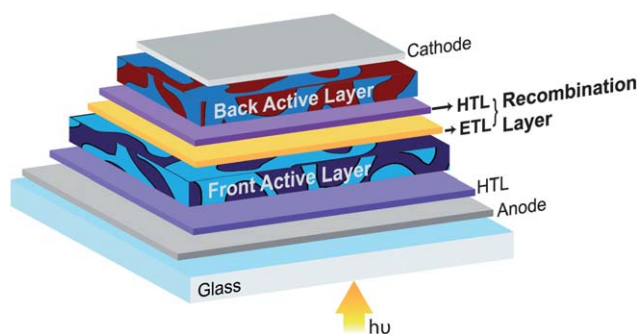


Fig. 1 Typical device structure for a solution-processed tandem polymer solar cell.

successfully fabricated with an inverted architecture, where electrons are collected at the ITO-coated glass and holes at the metal electrode.^{9–13} Although this article does not address the inverted tandem configuration, it can be assumed that the discussion relating to the CNO layer in a standard configuration is equally valid for an inverted architecture.

To date, titanium dioxide (TiO_2) and zinc oxide (ZnO) layers have been the predominant options for electron transport layers in organic photovoltaic devices, largely due to their transparency and solution-processability. TiO_2 has been touted as a robust diffusion barrier against oxygen and water, producing relatively air-stable polymer solar cells when incorporated,^{14,15} while ZnO solution-processed layers offer high electron mobility.¹⁶ However, the implementation of these materials into a tandem OPV device presents a challenge as TiO_x sol-gel derived layers are prone to cracks¹⁷ and ZnO -nanoparticle layers are sensitive to pH changes.^{18,19} Successful use of ZnO in tandem devices involved modification of the acidic poly(3,4-ethylenedioxythiophene):poly(styrenesulfonate), Pedot:PSS, dispersion (HTL) which decreases both the work function and conductivity of Pedot:PSS.¹⁹ There are no reports of cracks in films cast from ZnO nanoparticles probably because unlike sol-gel processed films, the ZnO nanoparticles were subjected to multiple washes after synthesis,²⁰ hence minimizing the amount of organic phase in the nanoparticle film. In contrast, sol-gel processed films will likely contain a significant amount of organic phase, which when removed during the drying/annealing process induces a large volume change in the film, resulting in cracks. We note from work done in our laboratory that films formed from ZnO nanoparticles and annealed at device temperatures (80 °C to 180 °C) remained somewhat porous at low film thicknesses (below *ca.* 25 nm), which often makes them poor barriers to some solvents.

In this work, we explore the use of perovskite, (TBA,H) $\text{Ca}_2\text{Nb}_3\text{O}_{10}$ ($E_g = 3.53$ eV (ref. 21)), nanosheets as a possible ETL candidate for the recombination layer. The well-known donor-acceptor BHJ system, poly(3-hexylthiophene) (P3HT) and (6,6)-phenyl- C_{61} -butyric acid methyl ester (PCBM), are used in the photoactive layer. The nanosheets have an indirect bandgap²² and have been shown to have favorable charge-separation properties through its utilization as a successful photocatalyst in the reduction of water to molecular hydrogen under UV illumination.^{21,23} The sheets are obtained by chemical exfoliation from the Dion-Jacobson phase $\text{K}_2\text{Ca}_2\text{Nb}_3\text{O}_{10}$. This layered perovskite

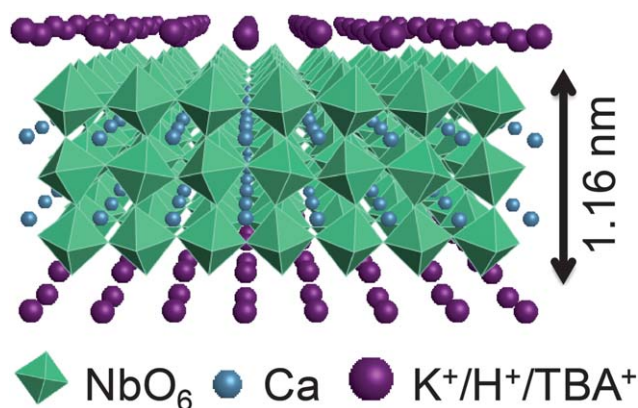


Fig. 2 Schematic structure of a $\text{Ca}_2\text{Nb}_3\text{O}_{10}^-$ layer and surrounding cations.

consists of alternating layers of potassium ions and anionic $\text{Ca}_2\text{Nb}_3\text{O}_{10}^-$ slabs, as shown in Fig. 2. The latter are built from corner shared NbO_6 octahedra, with Ca^{2+} ions in the voids. Chemical exfoliation replaces the potassium ions with more soluble tetrabutylammonium (TBA) ions, which allows extraction of the $\text{Ca}_2\text{Nb}_3\text{O}_{10}^-$ slabs into water and other polar solvents. During this process, the structure of the sheets and their thickness of 1.16 nm remain unchanged.²⁴ For simplicity, (TBA,H) $\text{Ca}_2\text{Nb}_3\text{O}_{10}$ will be referred to as CNO thereafter. The size of the nanosheet has been shown to have an effect on its optical and electronic properties;²² hence this can be used as another design parameter for future improvements.

2 Results and discussion

2.1 Mechanical properties

Sol-gel processed TiO_x films have been shown to be sensitive to relative humidity,^{25–27} and subsequent drying and thermal treatment.^{17,26} Film densification and microstructural changes during the spin-coating process result in significant tensile stress in the TiO_x film. This stress is further exacerbated if the film is then subjected to thermal treatment, causing cracks in the layer, as shown in Fig. 3. These defects are undesirable in a solution-processed solar cell, not only because of reduced electrical performance within the TiO_x layer but they are also detrimental to subsequent layer deposition as the solvent from the deposition of the second BHJ layer can penetrate into the cracks and dissolve the first BHJ layer. While high quality TiO_x films can be attained through rigorous control of the casting and post-processing environment, this may not be feasible for a scaled-up roll-to-roll process. Cracks in sol-gel processed layers are not only confined to TiO_x , they have also been observed in V_2O_5 hole transport layers.²⁸ The authors used V_2O_5 in the recombination stack for roll-to-roll processed tandem devices and noted that the cracked V_2O_5 layer renders it penetrable to solutes of subsequent deposition, leading to partial dissolution of underlying layers and consequently poor devices.²⁸ They postulated that the cracks formed either due to heat-treatment or mechanical stress (from substrate bending) during roll-to-roll processing.

CNO semiconductor nanosheets absorb in the ultraviolet (UV) region of the spectrum with an absorption band edge at

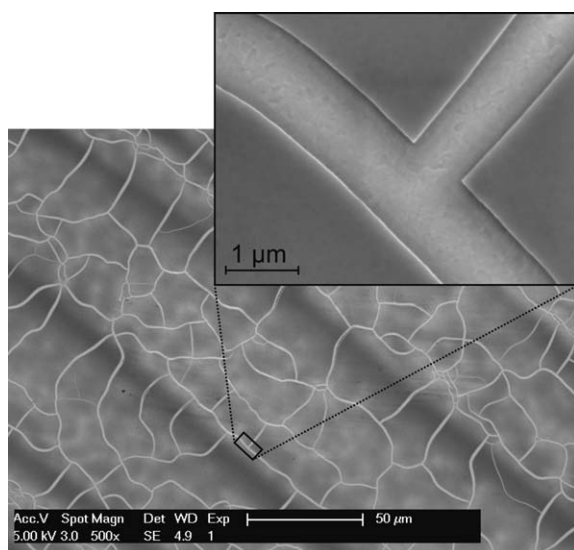


Fig. 3 SEM image of a cracked TiO_x layer on top of the BHJ film. The sample was annealed at 80°C for 10 minutes.

350 nm.²¹ As prepared, the flat nanosheets have a mixture of straight and irregularly shaped edges, with edge lengths varying from 0.2 μm to 1.8 μm .²¹ Transmittance and diffuse reflectance data of CNO films on quartz (see ESI, Fig. S1†) show that it is relatively transparent to the visible wavelength range at thicknesses below 150 nm.

When the nanosheets were spin-coated onto a hydrophobic P3HT:PCBM BHJ layer from isopropanol (a low surface energy, polar solvent of choice instead of water), we observed that the nanosheets do not uniformly coat the BHJ surface, as evidenced by the aggregation of nanosheets in the top left corner of the AFM (topography and phase) images in Fig. 4(a) and (b), and the exposed BHJ surfaces in the greater part of the images. Despite adequate initial wetting of the BHJ surface with the nanosheet-isopropanol dispersion, the nanosheets aggregate as the solvent evaporates during the spin-coating process. We suspect that the higher surface energy of the nanosheets prevents them from fully wetting the lower surface energy BHJ layer. However, when the BHJ layer was first exposed to nitrogen plasma¹³ for 2 seconds prior to CNO deposition, the nanosheets appear to uniformly coat the BHJ layer, as shown in both the topography and phase images, Fig. 4(c) and (d), respectively. Control experiments showed that nitrogen plasma does not adversely affect the performance of the active layer (see ESI, Fig. S2†).

Fig. 4(e) and (f) show a 5 μm by 5 μm AFM topography and phase images of CNO spin-coated from water onto a sol-gel derived TiO_x layer. The resulting CNO layer consists of nanosheets that were either lying flat against or at an angle from the TiO_x surface, with a root mean square (RMS) surface roughness of approximately 4 nm. The phase image in Fig. 4(f) seems to suggest discontinuous coverage of CNO (contrasting dark and bright areas throughout the figure). However, sectional analysis of line scans across the topography image, comparing them against the phase image, shows that the dark regions in the phase image corresponds to nanosheets that are not completely flat on the surface but are instead resting at an angle on the surface,

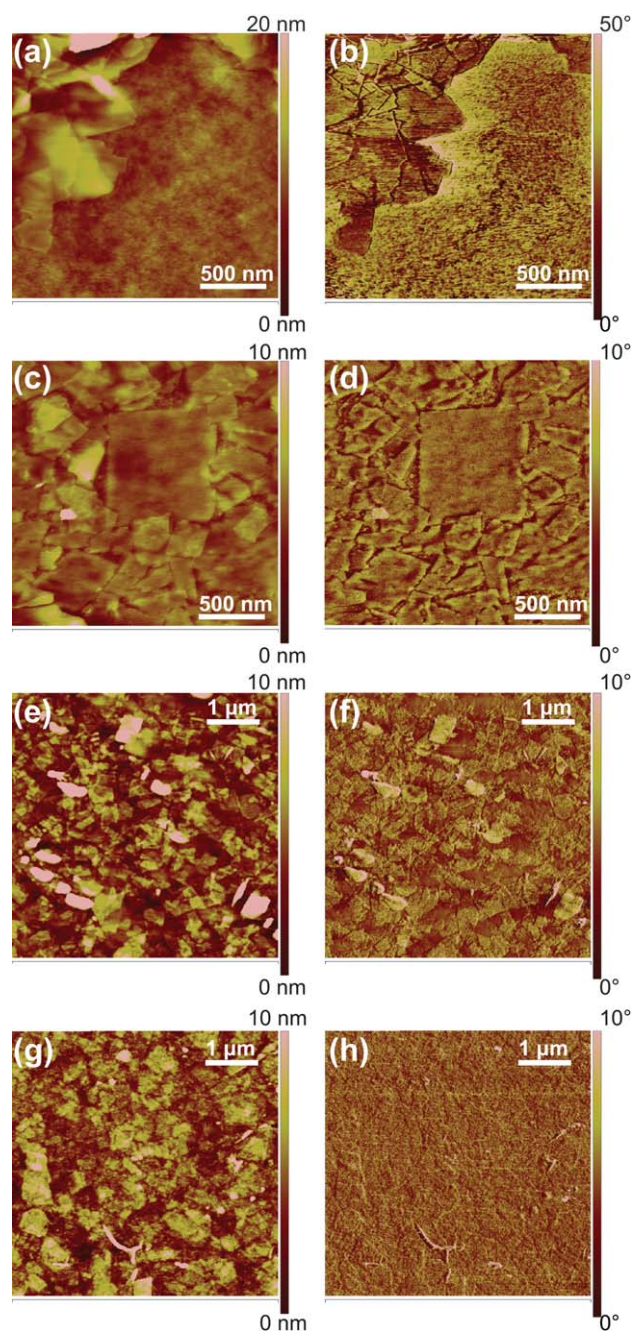


Fig. 4 AFM height (left: a, c, e and g) and phase (right: b, d, f and h) images of (a and b) CNO on the BHJ film spin-cast from isopropanol, (c and d) CNO on the BHJ film after N_2 plasma for 2 seconds, (e and f) CNO on the TiO_x film, and (g and h) after thin layer of Pedot:PSS deposition on CNO. Note: (a–d) are $2\ \mu\text{m} \times 2\ \mu\text{m}$ while (e–h) are $5\ \mu\text{m} \times 5\ \mu\text{m}$.

yielding a different phase-shift signal in sample-cantilever interaction (see ESI, Fig. S3†). Once formed, the CNO layer is stable towards subsequent layer depositions, as shown in Fig. 4(g) and (h), where it appears undisturbed after the deposition of a thin layer of Pedot:PSS (*ca.* 10 nm). The outlines of the individual nanosheets are still visible under the Pedot:PSS film in the topography image (Fig. 4(g)), while the RMS roughness of the surface decreased to approximately 2 nm.

2.2 Electronic properties and device characteristics

Fig. 5 shows the measured work function of materials used in constructing the recombination layers. The work function for TiO_x after heat treatment is not shown due to an aberrant measured value which is attributed to a discontinuous, cracked TiO_x layer as seen in Fig. 3. The work function of CNO was measured to be *ca.* 3.5 eV, and is almost unchanged after heat treatment at 150 °C for 5 minutes. The low work function of CNO makes it a good candidate for electron transport while its large band gap gives it excellent hole- and exciton-blocking capability. The measured work function of CNO lies close to the reported value for its conduction band edge²³ (after adjustments for the pH-change to the point of zero charge to approximate the flat band potential). This suggests a high density of mobile charge carriers when excited. In addition to its favorable energy level alignment, CNO is transparent for $\lambda > 350$ nm (see ESI, Fig. S1†). The combination of the AFM results and work function measurements depict CNO as a robust material that is amenable towards solution processing and post-processing treatment such as drying and heat-treatment.

In order to demonstrate that CNO can be used as an ETL in the recombination stack, tandem P3HT:PCBM BHJ devices were fabricated. The J - V characteristics of single-junction P3HT:PCBM BHJ devices are shown in comparison to tandem devices fabricated using different ETLs within the recombination stack (Fig. 6). With the exception of the ITO anode and the metal cathode, all of the layers within the devices were solution-deposited. It is relevant to note that the presented J - V traces are averaged over several devices and not from champion devices. The tandem devices were all heat treated at 150 °C for 5 minutes in a N_2 glove box (denoted as HT) and light-soaked under a solar simulator for 15 minutes (denoted as LS). All parameters for these devices are summarized in Table 1, and absorbance data for these devices are available in ESI, Fig. S4.† When TiO_x alone is employed as the ETL (without CNO), the V_{oc} is almost double that of a single junction device. However, the FF is very low (0.35) due to the manifestation of an S-kink in the J - V data that remained even after prolonged illumination with a solar simulator. This S-kink suggests an injection barrier for charges²⁹ which is likely the reason behind non-ohmic contact between

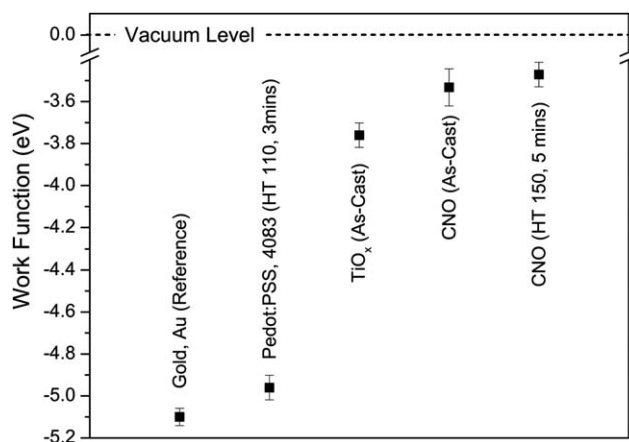


Fig. 5 Measured work function of Pedot:PSS, TiO_x , and CNO, with gold as reference.

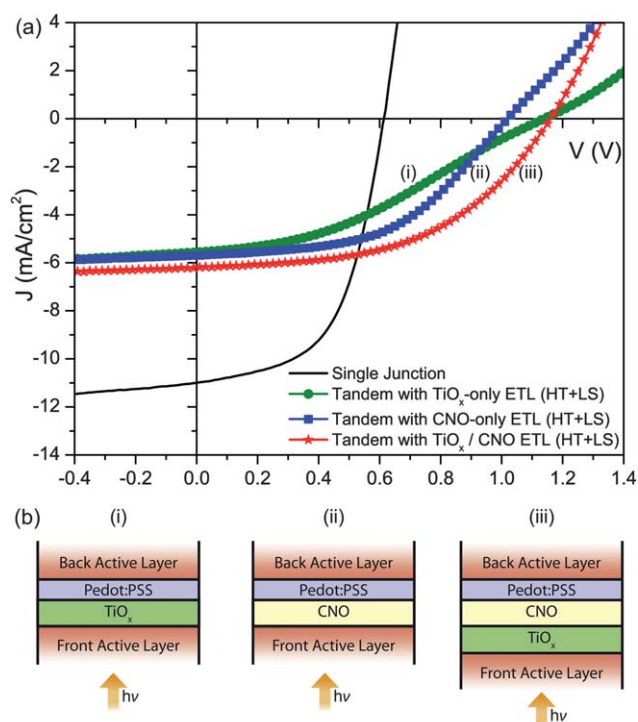


Fig. 6 (a) J - V curve (under illumination) comparing a P3HT:PCBM single junction device to various tandem devices with different ETLs within the recombination layer. A pictorial representation of the recombination stack corresponding to the J - V curves is shown in (b). (HT = heat treatment for 5 min at 150 °C, while LS = light-soaking under the solar simulator for 15 minutes.)

TiO_x and Pedot:PSS, as will be discussed in Fig. 8. When CNO alone (*ca.* 15 nm) is employed as the ETL within the recombination stack of a tandem device, the open-circuit voltage (V_{oc}) increases from 0.61 V for a single junction device to 1.02 V with a fill factor (FF) of 0.50, validating the electron transport property of the CNO layer. The V_{oc} is less than double that of a single junction device due to leakage (dark) current through the CNO. In the employed device geometry, it is impossible to distinguish if the leakage is due to a physical effect, *i.e.* intercalation of some of the subsequently deposited Pedot:PSS into intersheet gaps, or an electronic effect. Since the measured thickness of the CNO layer is an order of magnitude higher than the thickness of a single CNO nanosheet, we would expect the layer to be comprised of multi-layers of stacked CNO nanosheets, leading to non-uniform layer thicknesses, and consequently non-uniform electronic properties, especially in areas where the effect from surface defects (on the nanosheets) dominates. This leakage is minimized when TiO_x is first spin-coated onto the front sub-cell prior to the deposition of CNO, resulting in an improved V_{oc} of 1.16 V, with a FF of 0.50.

The manifestation of the S-shaped kink in the J - V curve of OPV devices incorporating TiO_x layers has been previously reported and the shape of the J - V curve has been shown to improve upon exposure to UV light.^{30–32} We observed a similar S-kink in our tandem devices with TiO_x within the ETL, as shown in the inset in Fig. 7. Light-soaking the device under the solar simulator for 15 minutes improved the J - V curve of the devices. In contrast, the S-kink is absent in the CNO-only

Table 1 Summary of device parameters for P3HT:PCBM BHJ devices shown in Fig. 6. The series resistances ($R_{s,est}$) are approximated from the slope of the $J-V$ curve at V_{oc} . (HT = heat treatment for 5 min at 150 °C, while LS = light-soaking under the solar simulator for 15 minutes)

Recombination layer	V_{oc}/V	$J_{sc}/\text{mA cm}^{-2}$	FF	PCE/%	$R_{s,est}/\Omega \text{ cm}^2$
None (single junction device)	0.61	10.99	0.56	3.75	12.7
TiO _x /Pedot:PSS (HT + LS)	1.14	5.57	0.35	2.22	167.0
CNO/Pedot:PSS (HT + LS)	1.02	5.70	0.50	2.91	72.4
TiO _x /CNO/Pedot:PSS (HT + LS)	1.16	6.19	0.50	3.59	51.5

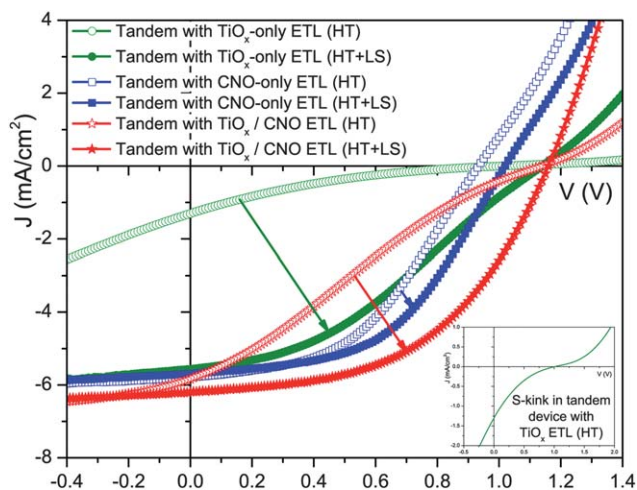


Fig. 7 $J-V$ curve (under illumination) comparing tandem devices before and after light-soaking under the solar simulator for 15 minutes (LS). HT refers to heat treatment for 5 min at 150 °C. The inset is the expanded range for the tandem device with TiO_x-only ETL where a distinct S-kink is present.

(square symbol) devices. Light-soaking for 15 minutes further improved the FF and the V_{oc} of the CNO-incorporated devices. This may be due to a trap-filling effect which has previously been observed at high excitation fluence in transient absorption study

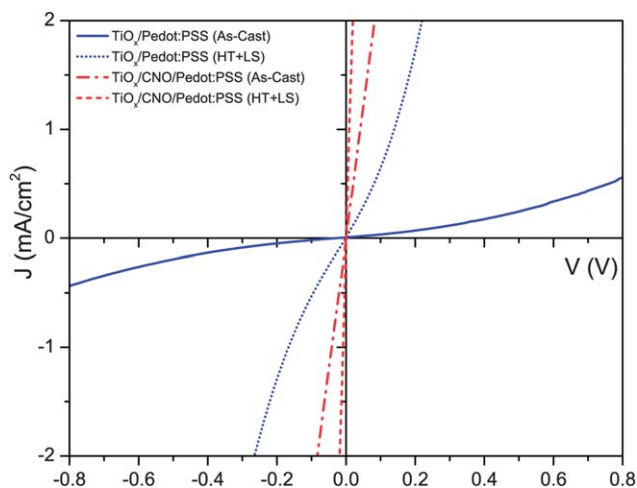


Fig. 8 $J-V$ curve (under illumination) comparing TiO_x/Pedot:PSS interconnect and TiO_x/CNO/Pedot:PSS interconnect. (HT = heat treatment for 5 min at 150 °C, while LS = light-soaking under the solar simulator for 15 minutes.)

of CNO nanosheets,²² *i.e.* trap density is reduced during prolonged photoexcitation of CNO, leading to a higher density of free charges. Other possible reasons include thermal detrapping of electrons from defect states (electron traps) due to an increase in device temperature during illumination. Notably, the S-kink which appeared in the TiO_x-only device is considerably suppressed when CNO is sandwiched in between TiO_x and Pedot:PSS. The S-kink in TiO_x and ZnO devices has been associated with chemisorbed O²⁻, while UV illumination leads to the desorption of O₂, hence resulting in mobile electrons.^{31,33} The suppression of the S-kink when CNO is used in tandem with TiO_x suggests that holes are being scavenged from the CNO layer for desorption of O₂ from TiO_x, *i.e.* electrons are being injected into the CNO layer. Also notable is that the slope of the $J-V$ curve near V_{oc} for the CNO-only tandem devices remained almost unchanged before and after light-soaking (*i.e.* the traces are parallel to each other near V_{oc}), suggesting minimal changes in series resistance. In contrast, tandem devices that employ TiO_x in the ETL showed an appreciable decrease in series resistance after light soaking. This observation is further substantiated in Fig. 8.

It has been shown that exfoliated CNO nanosheets can be readily restacked by changing the pH of the colloidal suspension, and the structure of exfoliated-restacked CNO nanosheets has been previously characterized.³⁴⁻³⁶ Since Pedot:PSS (pH 1.2) is spin-coated on top of the CNO layer in the tandem device, contact with the acidic dispersion likely caused the CNO nanosheets to restack. The band-gap energy of restacked CNO has been estimated to be 3.50 eV from optical studies and the conduction band edge approximated at -0.52 V (*vs.* NHE, at pH 0),³⁶ which is *ca.* -4.18 eV (*vs.* vacuum). Studies have shown a Nernstian dependence of the conduction band edge (flatband) to solution pH for metal oxides such as TiO₂, where the conduction band edge shifts to lower energy (*vs.* vacuum) as pH decreases.^{37,38} The lowering of the conduction band edge of CNO due to subsequent deposition of acidic Pedot:PSS makes the CNO favorable to accepting electrons from PCBM (LUMO = -4.1, *vs.* vacuum³⁹), even though initial assessment of the energy levels shows an energy barrier for electron transfer from PCBM to unstacked CNO nanosheets. Restacking is also thought to increase the density of surface defects.²¹

In order to isolate and study the recombination layers, we fabricated TiO_x/Pedot:PSS and TiO_x/CNO/Pedot:PSS devices with ITO as the electron-extracting electrode, and Ni/Ag as the hole-collecting electrode. P3HT:PCBM BHJ layers were deliberately excluded. Contact resistances from the electrodes can be disregarded since all devices have ITO/TiO_x for electron collection and Pedot:PSS/Ni for hole collection. $J-V$ traces under illumination are shown in Fig. 8. In the case of the

TiO_x/Pedot:PSS interconnect, the p–n junction acts as a counter diode and shows some rectification (Schottky contact), suggesting the presence of an injection barrier for electrons from TiO_x into Pedot:PSS. Exposure to UV light increases the free carrier concentration in TiO_x due to desorption of O₂,^{31,33} as previously mentioned, presumably allowing electrons to tunnel through energy barriers.³⁰ Although there was a decrease in the resistance of the layer stack after 15 minutes of light-soaking (LS), the TiO_x/Pedot:PSS contact did not become ohmic in any of our tests (Fig. 8). Some possible explanations include crack formation in the TiO_x layer, and an inadequate amount of UV light impinging upon the buried TiO_x layer since a solar simulator is used as an illumination source in our study, and the illumination is directed through a glass window, ITO-coated glass and photoactive layer which absorbed most of the UV light. We note however that a roll-to-roll fabricated tandem OPV would encounter a similar predicament if TiO_x were to be used within the buried recombination stack, making the S-kink an intractable problem for a commercial product.

When a layer of CNO (*ca.* 15 nm) is deposited between the TiO_x layer and the Pedot:PSS layer, the contact becomes ohmic even without light-soaking. The resistance of the interconnect with CNO sandwiched in between TiO_x and Pedot:PSS is further reduced after heat treatment and light-soaking, as evidenced by the increase in the slope of the *J–V* trace. Modification to the TiO_x–Pedot:PSS interface by inserting CNO nanosheets improved both the electron transport and the hole-blocking properties of the ETL components within the recombination stack. The S-shaped kink is suppressed as previously discussed, giving rise to an ohmic contact at the CNO–Pedot:PSS interface. Arguably, our tandem devices fabricated using a sol–gel TiO_x layer may not be comparable to published results,^{32,40} possibly due to insufficient illumination time/intensity, however, it is undeniable that the incorporation of CNO improved device performance.

While elegant transient absorption kinetic studies have been performed on CNO nanosheets in water and in the presence of a hole scavenger such as methanol,²² the findings may not fully extend to the sandwiched CNO layers in a tandem device, due to its complex electronic properties and sensitivity to its neighboring environment. However, we can draw several parallels that can help explain our system. Carroll *et al.* found that electrons become trapped faster compared to holes in the CNO nanosheets and postulated that the electron trap sites are located at the sheet edges (dangling Nb–O). The presence of trapped electrons in defect sites likely aids in the recombination with holes from Pedot:PSS, enhancing the function of the recombination stack. The study also confirms that excess photogenerated electrons are left on the CNO nanosheets in the presence of methanol (hole scavenger). We expect similar behavior when PCBM or TiO_x is in contact with the CNO layer due to holes preferentially moving towards PCBM or TiO_x. This is likely why the CNO/Pedot:PSS interconnect is ohmic.

To further illustrate the advantage of using CNO as an ETL, series resistances ($R_{s,est}$) were estimated from the slope of the *J–V* curve at V_{oc} (Table 1). It should be noted that this extracted $R_{s,est}$ value is not an absolute measurement but is proportional to the actual series resistance of the device. Extracting this value, however, provides us with another dimension of analysis. As expected, the $R_{s,est}$ was lowest for a single junction device,

followed by the tandem device employing the TiO_x–CNO combination as the ETL within the recombination stack. Devices with CNO-only showed almost comparable $R_{s,est}$, while devices with TiO_x-only had the largest $R_{s,est}$. This is consistent with the assertion of a lower density of mobile charge carriers in the TiO_x layer compared to the CNO layer.

3 Conclusions

We have demonstrated that a layer of CNO nanosheets is an excellent candidate for an ETL in a solution-processed multi-junction organic solar cell. The robust CNO layer can be spin-coated on top of a P3HT:PCBM BHJ photoactive layer and is stable toward subsequent processing and heat-treatment. CNO forms an ohmic contact with Pedot:PSS as-cast without requiring further UV treatment. The processability and electronic properties of this material make it very attractive for the envisioned large-scale solution-processing of OPV. The exploration of this perovskite material for PV is still in its infancy, and there are several hurdles that still need to be overcome. The origin of voltage loss in the CNO/Pedot:PSS interconnect still needs to be determined, and a more complete understanding of CNO interaction with neighboring layers still needs to be attained. However, despite the small losses in V_{oc} , we showed that we can achieve a V_{oc} of 1.02 and a FF of 0.50 in a tandem device employing CNO-only as the ETL, without extensive UV treatment. The absence of the S-kink in the CNO-only devices suggests that the mechanism for improvement of the *J–V* curve from light-soaking is different from that of devices employing TiO_x and ZnO. Drawing from past studies on CNO nanosheets, we postulate that trap-filling from prolonged light exposure decreases trap density and increases mobile carrier density in the CNO layer. In the case of TiO_x and ZnO, the reversibility of the *J–V* enhancement upon UV illumination has been associated with the reversible process of oxygen adsorption and desorption, hence the S-kink in the *J–V* curves reappears upon exposure to air.^{31,33}

Sol–gel derived TiO_x was used as an additional hole-blocking layer to demonstrate that the combined TiO_x–CNO ETL stack outperforms the individual material. The S-kink inherent in the *J–V* traces for TiO_x-devices is considerably suppressed when used in tandem with CNO. The CNO nanosheets overcame the weaknesses of the TiO_x layer by (1) minimizing the consequences of a cracked TiO_x layer and (2) increasing the mobile carrier density in the ETLs, while the TiO_x layer prevents leakage current through the CNO layer.

Uniformity of the CNO layer can potentially decrease leakage current through the layer. Further work is in progress in this area to understand the complex interaction between the CNO layer and its neighbors, and to isolate the reason(s) for the voltage losses in tandem devices employing a CNO/Pedot:PSS interconnect. In addition to its promise as an ETL candidate, these nanosheets can also be functionalized for linking of inorganic nanoparticles,⁴¹ which may become attractive for the exploitation of surface plasmons in PV devices.

4 Experimental

CNO nanosheets were synthesized according to published procedures.^{24,42} The white precipitates were collected through

centrifugation and washed several times with deionized water (18 M Ω). The nanosheets were suspended in either water or isopropanol. TiO_x sol-gel was synthesized from titanium isopropoxide (TIP) according to the published procedure¹⁵ and diluted in methanol for spin-coating to desired thicknesses.

Scanning electron microscope (SEM) images were collected using a Philips XL30 SFEG scanning electron microscope, using a beam energy of 5 kV and a working distance of 4.9 mm, under secondary electron detection. The SEM is equipped with energy-dispersive X-ray spectroscopy (EDAX) which was used to validate the absence of TiO_x within the cracks of the TiO_x film. Atomic force microscopy (AFM) measurements were acquired in tapping mode using a Veeco MultiMode 3 scanning probe microscope at a scan rate of 0.5 Hz. Silicon tips coated with 30 nm Al for enhanced reflectivity (Ted Pella, Inc.) with a spring constant of 40 N m⁻¹ were used for imaging. Images were analyzed and processed using Veeco's Nanoscope Analysis software. Work function values were measured with a Kelvin probe (KP Technologies, Inc.) under ambient conditions. Samples were prepared by spin-coating films onto ITO-coated glass. Work function values for aluminum with native oxide and UV-ozone gold were used to calibrate the work function of the probe tip. UV-vis measurements were conducted on a Thermo Scientific Evolution 220 UV-visible spectrophotometer equipped with an integrating sphere collection unit. Diffuse reflectance measurements were performed using a Teflon standard as the background; samples were positioned at an 8° angle from incident to minimize signal due to specular reflectance. Samples were prepared by spin-coating onto quartz slides.

Devices were fabricated on commercially available indium-tin oxide (ITO) coated glass with layer thickness of *ca.* 140 nm and 15 Ω sheet resistances. The substrates were first cleaned using chloroform followed by acetone, Mucosol detergent, and deionized water in an ultrasonic bath. They were then cleaned in a spin-rinse-dryer (SRD) system before being exposed to UV-ozone for 30 minutes. The ITO was first spin-coated with 40 nm of Pedot:PSS (Baytron P Al 4083, HC Starck). The Pedot:PSS coated samples were then heat-treated at 110 °C for 3 min and subsequently moved into a nitrogen glove box for deposition of the active layer. Both polymer and fullerene were dissolved in chlorobenzene and the solutions were stirred at 60 °C overnight before spin-coating to ensure that the polymer and fullerene has been completely dissolved. The active layer (thickness *ca.* 80 nm) was spin-coated from a 1 : 1 mixture of P3HT (Plextronics, M.W. \approx 75 kDa, reported regioregularity \geq 95%) and PCBM (Nano-C). The samples were then either spin-coated with sol-gel TiO_x (*ca.* 20 nm) or exposed to N₂ plasma for 2 seconds prior to spin-coating CNO (*ca.* 7 mg ml⁻¹ solution). Samples coated with TiO_x can be deposited with CNO without N₂ plasma. Subsequently, samples were coated with *ca.* 20 nm Pedot:PSS before spin-coating the second active layer (*ca.* 80 nm). After that, the samples were moved to a high vacuum chamber (*ca.* 10⁻⁶ mbar), where an electrode of 5 nm Ca and 150 nm Ag were vapor-deposited through a mask leaving six solar cells with an active area of 0.1690 cm². After metal deposition, the samples were either directly measured or annealed for 5 minutes at 150 °C prior to measurement in a N₂ glove box. For the study on the recombination layers, TiO_x was spin-coated on top of ITO (cathode), followed by CNO or Pedot:PSS, and Ni/Ag anodes

were vacuum deposited. The *I-V* curves of the samples were measured using a Keithley 2420 source measurement unit in a N₂ glove box. AM 1.5 illumination at 100 mW cm⁻² (1 SUN) was provided by a solar simulator (Radiant Source Technology). Reported efficiencies are not corrected for spectral mismatch. Sample thickness was determined using a Dektak surface profiler that was calibrated to a Si-SiO₂ ellipsometry standard.

Acknowledgements

The authors thank Plextronics for the generous donation of P3HT used in this study. We also thank René Janssen and Martijn Wienk for useful discussions and advice relating to the use of nitrogen plasma. This work is supported by the National Science Foundation Energy for Sustainability program, Award no. 0933435. Lilian Chang is supported by ConocoPhillips graduate fellowship.

References

- 1 B. A. Gregg and M. C. Hanna, *J. Appl. Phys.*, 2003, **93**, 3605–3614.
- 2 W. W. Kromhout, *UCLA Engineers Create Tandem Polymer Solar Cells that Set Record for Energy-Conversion*, 13 February 2012, <http://www.newsroom.ucla.edu/portal/ucla/ucla-engineers-create-tandem-polymer-228468.aspx>, accessed 14 March 2012.
- 3 R. Schueppel, R. Timmreck, N. Allinger, T. Mueller, M. Furno, C. Uhrich, K. Leo and M. Riede, *J. Appl. Phys.*, 2010, **107**, 044503.
- 4 M. Hiramoto, M. Suezaki and M. Yokoyama, *Chem. Lett.*, 1990, **19**, 327–330.
- 5 A. Yakimov and S. R. Forrest, *Appl. Phys. Lett.*, 2002, **80**, 1667–1669.
- 6 C. W. Tang, *Appl. Phys. Lett.*, 1986, **48**, 183–185.
- 7 G. Yu and A. J. Heeger, *J. Appl. Phys.*, 1995, **78**, 4510–4515.
- 8 T. Ameri, G. Dennler, C. Lungenschmied and C. J. Brabec, *Energy Environ. Sci.*, 2009, **2**, 347–363.
- 9 O. Hagemann, M. Bjerring, N. C. Nielsen and F. C. Krebs, *Sol. Energy Mater. Sol. Cells*, 2008, **92**, 1327–1335.
- 10 T. T. Larsen-Olsen, E. Bundgaard, K. O. Sylvester-Hvid and F. C. Krebs, *Org. Electron.*, 2011, **12**, 364–371.
- 11 L. Dou, J. You, J. Yang, C.-C. Chen, Y. He, S. Moriarty, K. Emery, G. Li and Y. Yang, *Nat. Photonics*, 2012, **6**, 180–185.
- 12 C.-H. Chou, W. L. Kwan, Z. Hong, L.-M. Chen and Y. Yang, *Adv. Mater.*, 2011, **23**, 1282–1286.
- 13 S. Kouijzer, S. Esiner, C. H. Frijters, M. Turbiez, M. M. Wienk and R. A. J. Janssen, *Adv. Energy Mater.*, 2012, **2**, 945–949.
- 14 K. Lee, J. Y. Kim, S. H. Park, S. H. Kim, S. Cho and A. J. Heeger, *Adv. Mater.*, 2007, **19**, 2445–2449.
- 15 D. H. Wang, S. H. Im, H. K. Lee, O. O. Park and J. H. Park, *J. Phys. Chem. C*, 2009, **113**, 17268–17273.
- 16 A. L. Roest, J. J. Kelly, D. Vanmaekelbergh and E. A. Meulenkaamp, *Phys. Rev. Lett.*, 2002, **89**, 036801.
- 17 M. Bockmeyer and P. Löbmann, *Thin Solid Films*, 2007, **515**, 5212–5219.
- 18 J. Gilot, M. M. Wienk and R. A. J. Janssen, *Appl. Phys. Lett.*, 2007, **90**, 143512.
- 19 D. J. D. Moet, P. de Bruyn and P. W. M. Blom, *Appl. Phys. Lett.*, 2010, **96**, 153504.
- 20 W. J. E. Beek, M. M. Wienk, M. Kemerink, X. Yang and R. A. J. Janssen, *J. Phys. Chem. B*, 2005, **109**, 9505–9516.
- 21 O. C. Compton, E. C. Carroll, J. Y. Kim, D. S. Larsen and F. E. Osterloh, *J. Phys. Chem. C*, 2007, **111**, 14589–14592.
- 22 E. C. Carroll, O. C. Compton, D. Madsen, F. E. Osterloh and D. S. Larsen, *J. Phys. Chem. C*, 2008, **112**, 2394–2403.
- 23 E. M. Sabio, R. L. Chamousis, N. D. Browning and F. E. Osterloh, *J. Phys. Chem. C*, 2012, **116**, 3161–3170.
- 24 A. J. Jacobson, J. W. Johnson and J. T. Lewandowski, *Inorg. Chem.*, 1985, **24**, 3727–3729.
- 25 J. Slunečko, M. Kosec, J. Holc, G. Dražić and B. Orel, *J. Am. Ceram. Soc.*, 1998, **81**, 1121–1124.
- 26 M. Burgos and M. Langlet, *J. Sol-Gel Sci. Technol.*, 1999, **16**, 267–276.

- 27 L. H. Slooff, J. M. Kroon, J. Loos, M. M. Koetse and J. Sweelssen, *Adv. Funct. Mater.*, 2005, **15**, 689–694.
- 28 T. T. Larsen-Olsen, T. R. Andersen, B. Andreasen, A. P. L. Böttiger, E. Bundgaard, K. Norrman, J. W. Andreasen, M. Jørgensen and F. C. Krebs, *Sol. Energy Mater. Sol. Cells*, 2012, **97**, 43–49.
- 29 A. Kumar, S. Sista and Y. Yang, *J. Appl. Phys.*, 2009, **105**, 094512.
- 30 T. Kuwabara, H. Sugiyama, T. Yamaguchi and K. Takahashi, *Thin Solid Films*, 2009, **517**, 3766–3769.
- 31 H. Schmidt, K. Zilberberg, S. Schmale, H. Flügge, T. Riedl and W. Kowalsky, *Appl. Phys. Lett.*, 2010, **96**, 243305.
- 32 S. Sista, Z. Hong, M.-H. Park, Z. Xu and Y. Yang, *Adv. Mater.*, 2010, **22**, E77–E80.
- 33 G. Lakhwani, R. F. H. Roijmans, A. J. Kronemeijer, J. Gilot, R. A. J. Janssen and S. C. J. Meskers, *J. Phys. Chem. C*, 2010, **114**, 14804–14810.
- 34 Y. Ebina, T. Sasaki and M. Watanabe, *Solid State Ionics*, 2002, **151**, 177–182.
- 35 F. F. Xu, Y. Ebina, Y. Bando and T. Sasaki, *J. Phys. Chem. B*, 2003, **107**, 9638–9645.
- 36 K. Maeda and T. E. Mallouk, *J. Mater. Chem.*, 2009, **19**, 4813–4818.
- 37 L. Kavan, M. Grätzel, S. E. Gilbert, C. Klemenz and H. J. Scheel, *J. Am. Chem. Soc.*, 1996, **118**, 6716–6723.
- 38 L. A. Lyon and J. T. Hupp, *J. Phys. Chem. B*, 1999, **103**, 4623–4628.
- 39 M. S. White, D. C. Olson, S. E. Shaheen, N. Kopidakis and D. S. Ginley, *Appl. Phys. Lett.*, 2006, **89**, 143517.
- 40 J. Y. Kim, K. Lee, N. E. Coates, D. Moses, T. Q. Nguyen, M. Dante and A. J. Heeger, *Science*, 2007, **317**, 222–225.
- 41 J. Y. Kim, F. E. Osterloh, H. Hiramatsu, R. K. Dumas and K. Liu, *J. Phys. Chem. B*, 2005, **109**, 11151–11157.
- 42 R. E. Schaak and T. E. Mallouk, *Chem. Mater.*, 2000, **12**, 2513–2516.